Planetary interior configuration control on thermal evolution and geological history.

L. H. Lark[1], C. Huber[1], E. M. Parmentier[1], and J. W. Head[1]

[1] Department of Earth, Environmental and Planetary Sciences, Brown University, Providence, Rhode Island, USA.

Corresponding author: Laura Lark (laura_lark@brown.edu)

Key Points:

- The distribution of heat-producing elements within a planetary mantle controls relative timing of volcanism, tectonism, and magnetism.
- The geological histories of the Moon and Mars suggest deep sequestration of heat-producing elements.
- The geological history of Mercury suggests shallow sequestration of heat-producing elements.

Abstract

The terrestrial planetary bodies display a wide variety of surface expressions and histories of volcanic and tectonic, and magnetic activity, even those planets with apparently similar dominant modes of heat transport (e.g., conductive on Mercury, the Moon, and Mars). Each body also experienced differentiation in its earliest evolution, which may have led to density-stabilized layering in its mantle and a heterogenous distribution of heat-producing elements. We explore the hypothesis that mantle structure exerts an important control on the occurrence and timing of geological processes such as volcanism and tectonism. We investigate numerically the behavior of an idealized model of a planetary body where heat-producing elements are assumed to be sequestered in a stabilized layer at the top or bottom of the mantle. We find that the mantle structure alters patterns of heat flow at the boundaries of major heat reservoirs: the mantle and core. This modulates the way in which heat production influences geological processes. In the model, mantle structure is a dominant control on the relative timing of fundamental processes such as volcanism, magnetic field generation, and expansion/contraction, the record of which may be observable on planetary body surfaces. We suggest that Mercury exhibits characteristics of shallow sequestration of heat producing elements and that Mars exhibits characteristics of deep sequestration.

Plain Language Summary

The surfaces of Mercury, the Moon, and Mars have been shaped by volcanism, global expansion and contraction, and the effects of magnetic fields. These three bodies also underwent differentiation shortly after they formed, possibly resulting in distinct layers within their mantles as well as preferential sequestration of the radioactive, heat-producing elements primarily in one layer. We delve into the hypothesis this layering plays a pivotal role in determining when geological processes such as volcanic eruptions and global expansion and contraction can occur. We use numerical models to simulate heat transport processes in a simplified planet with the heat-producing elements sequestered in a stabilized layer either at the top or the bottom of the mantle. We find that layering in the mantle and sequestration of heat-producing elements changes the way that a planet's mantle exchanges heat with the planet's core and the surface, influencing the relative timing of volcanic activity, global tectonics, and magnetic field generation, all of which can leave observable imprints on planetary surfaces. We propose that

Mercury's geological history is consistent with heat-producing elements locked into a layer at the top of its mantle, whereas the geological history of Mars is consistent with a deeper distribution.

1 Introduction

The surfaces of the terrestrial planetary bodies record a wealth of information about their geologic histories, especially their volcanic, tectonic, and magnetic activity. To connect these geological histories to the evolution of the planets, it is important to identify the major parameters which characterize planetary evolution and map out evolutionary regimes and their geological consequences within this parameter space.

While the presence of plate tectonics on Earth (and possibly ancient Venus) complicates comparison to the one-plate bodies (Mercury, the Moon, and Mars), there is substantial variability in the timing, activity, and style of volcanism, global tectonism, and magnetic field generation for the single-plate bodies alone (e.g., Solomon, 1978; Carr and Head, 2010; Tosi and Padovan, 2021; Tikoo and Evans, 2022). The Moon and Mercury experienced flood volcanism which peaked after an early period of low activity (and an earlier stage of crust-building) and then waned over billions of years (Byrne et al., 2016; Head et al., 2023) whereas the volcanic history of Mars (Carr and Head, 2010) prominently features plume-style volcanism which built enormous volcanic provinces and associated edifices such as Olympus Mons (Werner et al., 2009). Both the Moon (Tikoo and Weiss, 2014) and Mars (Acuna et al., 1999) generated strong early magnetic field dynamos that are not presently active. Mercury, on the other hand, has a magnetic field today and crustal remanent magnetization provides evidence for a magnetic field throughout much of Mercury's evolution (Ness, 1979; Johnson et al., 2016). Tectonically, Mercury's surface is cut by many wrinkle ridges, interpreted to indicate substantial global contraction beginning in its early history (Watters and Nimmo, 2010; Byrne et al., 2014; Watters et al., 2015; Crane and Klimczak, 2017). The Moon experienced expansion in its early history (Solomon and Head, 1980; Andrews-Hanna et al., 2013), with limited global contraction occurring later (Nahm et al. 2023). Interpretation of Mars's tectonic history is complicated by volcanic resurfacing but there is evidence of both expansion and contraction (Nahm and Schultz, 2011; Andrews-Hanna and Broquet, 2023). This observable variations in magnetic, volcanic, and

78 tectonic (expansion/contraction) activity provides the opportunity to evaluate these three bodies
79 comparatively in order to understand the dominant factors which led to divergence in their
80 evolutions.

81 Mercury, the Moon, and Mars also vary widely in chemical composition, notably in
82 metal-silicate ratio and in oxygen fugacity, which exerts an important control on mantle
83 geochemistry (Cartier and Wood, 2019). Separation of different phases during early
84 differentiation of the mantle can produce heterogeneity in both bulk composition and trace
85 element content (Figure 1). For the Moon and Mars, magma ocean solidification would have co-
86 concentrated the heat producing elements (HPE: uranium, thorium, and potassium) with high-
87 density iron; this process is suggested to have formed the KREEP material on the Moon (Warren
88 and Wasson, 1979) and a deep heated layer on Mars (Elkins-Tanton et al., 2003). On Mercury,
89 solidification of its highly reduced, iron-poor magma ocean likely co-concentrated HPE with
90 low-density sulfur, potentially even forming HPE-rich sulfides (Boukare et al., 2019). The
91 variation of density in magma ocean cumulates could plausibly result in stabilized long-term
92 mantle layering (Kellogg et al, 1999; Tosi et al., 2013; Zhang et al., 2017), sequestering HPE at

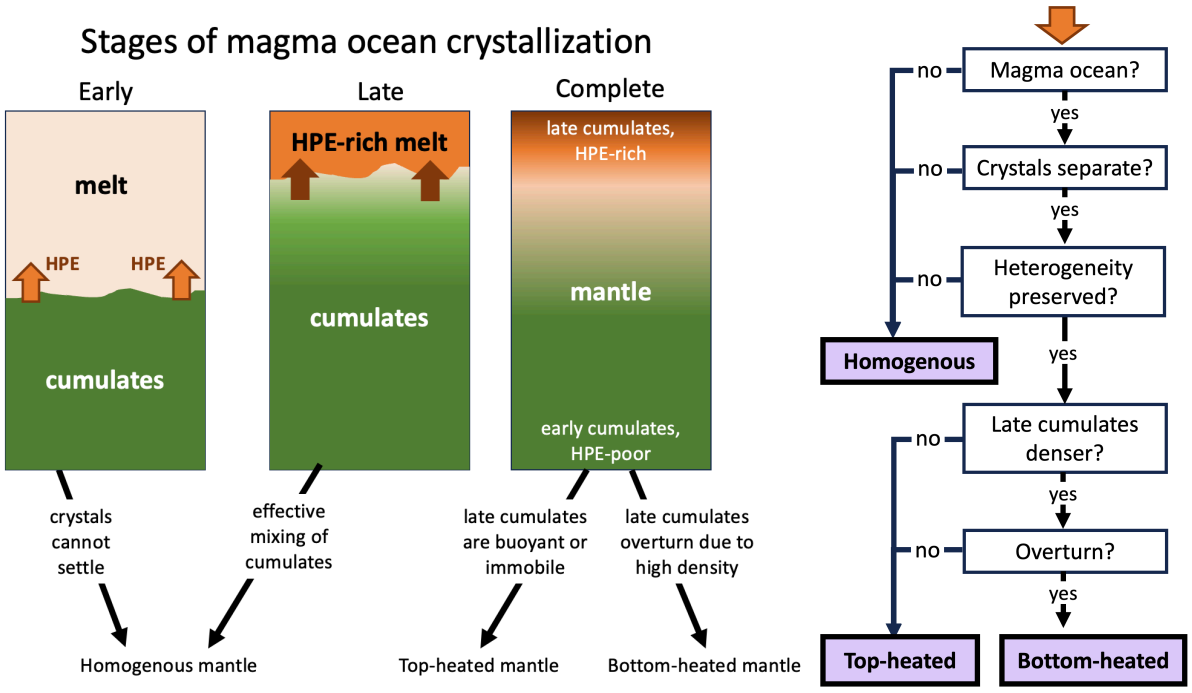

Figure 1. Schematic diagram of the generation of stable compositional structure in the mantle through crystallization of a magma ocean, including deep or shallow sequestration of heat-producing elements.

93 the top or bottom of the mantle over large portions of a planet's history. Figure 1 illustrates how
94 differentiation through a magma ocean phase might result in a layered mantle, depending on
95 whether crystals can physically separate from the melt, whether late cumulates are denser or less
96 dense than early cumulates, and whether heterogeneity can be preserved despite later mantle
97 convection.

98 The resulting distribution of HPE is particularly important for subsequent geodynamical
99 evolution. Predictions of the geological and geodynamical consequences of sequestered HPE
100 exist for several specific scenarios. The influence of HPE-rich material at the core-mantle
101 boundary on magnetic field generation, global tectonics, and volcanism has been explored for the
102 Moon (Stegman et al., 2003; Zhang et al., 2013; Hess and Parmentier, 1995) and Mars (Elkins-
103 Tanton et al., 2005; Plesa et al., 2014; Samuel et al., 2021); deep HPE have a particularly strong
104 influence on core evolution. Partial shallow sequestration of HPE by incorporation of HPE-rich
105 material in the lithosphere has been explored for Mercury (Peterson et al., 2021), the Moon
106 (Wieczorek and Phillips, 2000), and Mars (Plesa et al., 2018); these treatments show that mantle
107 convective evolution is especially affected. Collectively, these themes demonstrate that the
108 spatial distribution of HPE can have enormous influence on the timing and vigor of geological
109 processes that are driven by heat transfer, including volcanism, magnetic field generation, and
110 global tectonic processes such as expansion and contraction. These results have motivated us to
111 undertake a more generalized evaluation of the influence of compositional structure, and in
112 particular of sequestered heating, on planetary geological evolution among different planetary
113 bodies.

114 We present a first step toward such a picture, with a focus on situations in which heat
115 transport has been dominated by heat conduction and mantle solid-state convection (vs. plate
116 tectonics or volcanic heat-piping). We conceptualize a planet's high-level magnetic, volcanic,
117 and tectonic evolution through four geologically important transitions:

118 (1) The development of solid-state mantle convection,

119 (2) The cooling of the mantle to be sub-solidus everywhere,

120 (3) The onset of core cooling, and

121 (4) The onset of net planet cooling (surface heat loss exceeds internal heat production).

Transitions (1) and (2) define two phases of potential mantle melting with very different predicted surface expressions according to the source of energy for melt production. Transition (3) marks the beginning of conditions favorable for magnetic field generation, while transition (4) approximates the time of transition from planetary global net expansion to net contraction. The relative timing of transitions (1)-(4) provides a framework to evaluate the coexistence and therefore potential for interaction between magnetic, volcanic, and tectonic activity. For example, a planet in which the core begins to cool before the mantle becomes subsolidus might retain a remanent magnetic signature in its volcanic deposits, whereas no contemporaneous volcanic and magnetic activity is possible if the mantle is subsolidus by the time core cooling begins. Similarly, if a planet begins to cool before (2), one or both volcanic eras may occur in a state of lithospheric compressional stress; if the transition from warming to cooling occurs after (2), volcanism should occur in a state of lithospheric extension.

To understand the influence of planetary compositional structure on the relative timing of the geologically important transitions, we explore the concentration of heat production at the top or bottom of the model mantle, varying widely its intensity as well as other important parameters such as mantle Rayleigh number and core size; results are given in Section 3. The simplicity of the model permits investigation of the influence of the model planet structure on the resulting evolution, presented in Section 4. Finally, in Section 5, we discuss the implications of our findings for terrestrial planets and whether the disparate geological evolutions of Mercury, the Moon, and Mars might be a consequence of their bulk geochemistry and early differentiation.

2 Methods

As part of this work, we aim to define the important parameters characterizing planetary evolution in light of potential mantle layering resulting from early differentiation. We approach this goal by evaluating the evolution of a highly simplified planet. We first present our conceptual model of an idealized planet, then describe the physical model that we use to evaluate its evolution, followed by the details of our numerical implementation of the physical model. Finally, we describe the parameter space that we explore.

2.1 Conceptual model: We consider a planet to consist of a region representing the mantle through which heat may be transported by thermal convection or conduction overlying a

heat reservoir representing the core. We compare three endmember scenarios for mantle structure, which are illustrated in Figure 2: a) one homogenous scenario in which the mantle is fully mobile and uniformly heated, b) one layered scenario in which all HPE are concentrated in an immobile layer at the top of the mantle, and c) another layered scenario in which all HPE are concentrated in an immobile layer at the bottom of the mantle.

2.2 Physical model: We model the evolution of the idealized mantle using a thermal convection model, which is 2-D and time-dependent. We ensure that we are in the incompressible Stokes regime, in which inertia and compressibility effects are unimportant. Velocities are enforced to be zero in the stabilized layer, if present. Volumetric heating may be spatially heterogenous and decays exponentially over time. The core is modeled as an isothermal heat reservoir, with a constant temperature which is equal to its heat content divided by its total heat capacity. The evolution of the system is governed by the conservation of mass, momentum, and heat, described by equations 1-4 in dimensionless form:

$$\nabla \cdot \bar{u}^* = 0 \tag{1}$$

$$\nabla^2 \bar{u}^* - \nabla P^* + Ra \cdot T^* \cdot \hat{e}_z = 0 \tag{2}$$

$$\frac{\partial T^*}{\partial t^*} + (\bar{u}^* \cdot \nabla) T^* = \nabla^2 T^* + \frac{\tau_D}{\tau_H} \cdot f(z^*) \cdot 2^{-\frac{\tau_D}{\tau_{1/2}} t^*} \tag{3}$$

$$\frac{\partial {T_c}^*}{\partial t^*} = \frac{1}{C} \cdot \frac{\partial {Q_c}^*}{\partial t^*} \tag{4}$$

where $\bar{u}^*$ is velocity, P^* is pressure, T^* is mantle temperature, $\hat{e}_z$ is the unit vector in the direction of gravity, t^* is time, $\mathrm{T_c}^*$ is core temperature, and $\mathrm{Q_c}^*$ is core sensible heat (asterisks indicating nondimensionalized variables). $C = \frac{C_c}{C_m}$ is the total heat capacity of the core relative to

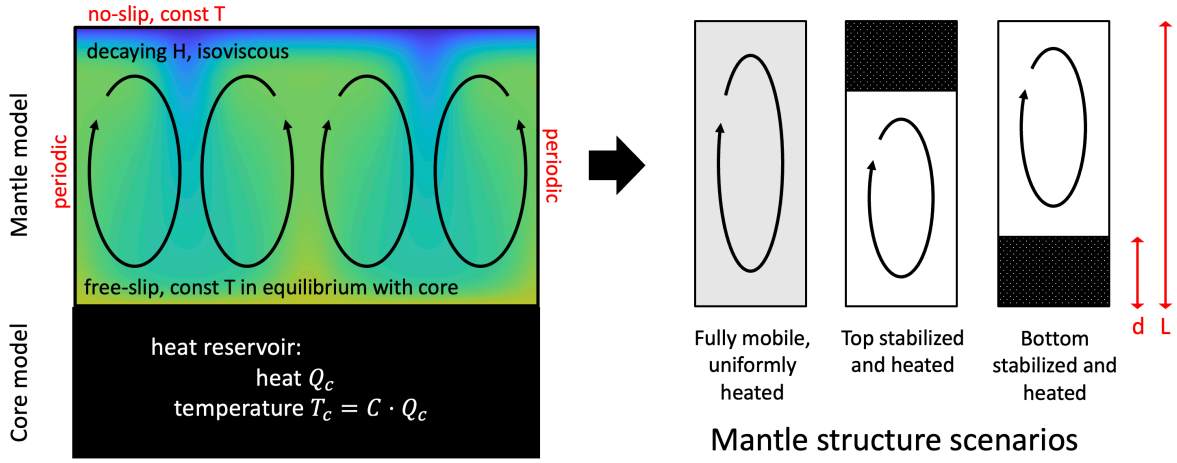

Figure 2. Conceptual sketch of model setup and illustration of mantle structure scenarios.

that of the mantle. The Rayleigh number is $Ra = \frac{\rho g \alpha \Theta L^3}{\mu \kappa}$ where ρ is mantle density, g is acceleration due to gravity, α is mantle thermal expansivity, Θ is a characteristic temperature, L is the scale length of the mantle (the height in rectangular geometry, or the volume divided by the surface area in a curved body), μ is mantle viscosity, and κ is mantle thermal diffusivity. The spatial distribution of HPE is described by a function f, which for the homogenous scenario is equal to 1 everywhere and for the layered scenarios is equal to L/d in the heated layer and zero elsewhere. Each τ is a characteristic timescale of the system; $\tau_D = \frac{L^2}{\kappa}$ is the mantle diffusive timescale; $\tau_H = \frac{\Theta C_m}{H_0}$ is the radiogenic heat production timescale where H_0 is the initial total volumetric heating rate (longer means weaker heating); $\tau_{1/2}$ is the radiogenic half-life (longer means slower decay). All symbols are also defined in Table 1.

The top boundary of the system is maintained at a constant temperature to reflect radiative equilibrium at the planet's surface. As in a one-plate planet with a liquid outer core, the flow boundary conditions are no-slip at the top and free-slip at the bottom. The left and right boundaries are periodic for both temperature and velocity. The core and mantle are coupled by continuity of heat flux and temperature at the bottom boundary of the mantle; heat flux changes core heat while the evolving core temperature is used to set the mantle bottom temperature. The mantle and core initially have the same uniform temperature, Θ (slightly perturbed to allow

instabilities to develop), reflecting a well-mixed thermal state following magma ocean solidification.

2.3 Model parameterization: Equations (1)-(4) imply that the behavior of the system is governed by five nondimensional numbers: the Rayleigh number, τ_D/τ_H, d/L, $C = C_c/C_m$, and $\tau_D/\tau_{1/2}$. To understand the influence of each nondimensional number, we computed the evolution of 150 models with parameters chosen from a range of values appropriate for the terrestrial planetary bodies, summarized in Table 2. The Rayleigh number controls the relative influence of conductive and convective heat transport in the mantle (higher values mean more convective transport). We explore sluggish to moderately vigorous convection ($Ra = 10^4 - 10^6$) to encapsulate variation in properties such as mantle viscosity, acceleration due to gravity, and mantle thickness. The ratio τ_D/τ_H controls the relative influence of heat transport and radiogenic heat production (higher values mean stronger heat generation). We explore heat production ranging from none to very strong ($\tau_D/\tau_H = 0, 3.8, 7.7, 11.5,$ and 15.4); heating may be distributed uniformly or concentrated into the stabilized layer at the top or bottom of the mantle (i.e., three configuration scenarios). We consider a thick or thin

	Symbol	Units	Meaning
Physical properties	α	-	thermal expansivity
	C_m, C_c	J/K	mantle, core total heat capacity
	g	m/s^2	gravitational acceleration
	H_0	W	initial total rate of volumetric heating
	κ	m^2/s	thermal diffusivity
	L	m	mantle height
	μ	Pa·s	mantle viscosity
	ρ	kg/m^3	mantle density
	Θ	K	initial temperature
System properties	$C = \frac{C_c}{C_m}$	-	core size (relative heat capacity)
	d/L	-	immobile mantle fraction
	$f = 1$ or $f = 0, L/d$	-	spatial HPE distribution
	$Ra = \frac{\rho g \alpha \Theta L^3}{\mu \kappa}$	-	Rayleigh number
	$\tau_{1/2}$	s	radiogenic decay half-life
	$\tau_D = \frac{L^2}{\kappa}$	s	mantle diffusive timescale
	$\tau_H = \frac{\Theta C_m}{H_0}$	s	radiogenic heat production timescale
Model variables	$P^* = P\,\tau_D/\mu$	-	pressure
	$Q_c{}^* = Q_c/\Theta C_m$	-	core sensible heat
	$t^* = t/\tau_D$	-	time
	$T^* = T/\Theta$	-	mantle temperature
	$T_c = T_c/\Theta$	-	core temperature
	$\bar{u}^* = \bar{u}\,\tau_D/L$	-	velocity
	$z^* = z/L$	-	vertical coordinate

Table 1. Meanings of symbols used.

Parameter	Meaning	Values considered
Ra	Rayleigh number	$10^4, 10^5, 10^6$
τ_D/τ_H	Heating strength	0, 3.8, 7.7, 11.5, and 15.4
d/L	Stabilized layer thickness	$1/8, 1/4$
C	Core size (heat capacity)	0.2, 2

Table 2. Varied parameters. Three models (top-heated, bottom-heated, and homogenous) were run for each combination.

stabilized layer ($d/L = \frac{1}{8}, \frac{1}{4}$) and a small or large core relative to the mantle, in terms of heat capacity ($C = 0.2, 2$). We do not vary the size of the mantle, so variation in the core total heat capacity is coupled to variation in planet size; because we are not investigating core cooling beyond the time of onset, this coupling does not appear to be very important. Finally, we consider a fixed half-life of radiogenic decay relative to the diffusive timescale ($\tau_D/\tau_{1/2} = 6.3$); this number controls the degree to which radiogenic heat can build up (high values mean that heat can build up). With a radiogenic decay half-life of 1.75 Gy and a rectangular mantle with a thermal diffusivity of 10^{-6} m^2/s, this value corresponds, for example, to a planet with a mantle thickness of 600-1800 km ($\tau_D/\tau_{1/2} = 1$ with a mantle thickness of approximately 240 km). Alternatively, $\tau_D/\tau_{1/2} = 6.3$ for a radiogenic decay half-life of 0.7 My and a mantle thickness of 12-36 km. A high value of $\tau_D/\tau_{1/2}$ ensures that our models run in a regime where radiogenic heat can build up; the terrestrial planetary bodies all have mantles much thicker than 240 km, so they are all in this regime. We note that direct scaling of our model evolutions to a much larger planet would necessarily imply unrealistically long-lived radiogenic heat production. However, our primary conclusions concern the limiting heat transport processes in different scenarios; we expect these to be relevant within the regime of large $\tau_D/\tau_{1/2}$.

In order to isolate the influence of mantle structure on the model's evolution, our idealized planet model includes three important simplifying assumptions. We have designed our numerical experiments in such a way that our results nevertheless provide insights as to the interaction of mantle structure with features of a more complex system. First, we assume that viscosity and thermal conductivity are constant in the mantle. Our calculations consider a range over two orders of magnitude in mantle viscosity (through its influence on the Rayleigh number), allowing us to relate our results to the behavior of a system that becomes more viscous as it cools, while

237 the top-heated scenarios provide insight into the insulating effects of crust/regolith/stagnant lid
238 development. Second, we model the mantle in cartesian geometry. The effects of planetary
239 curvature, which alters the relative efficiency of extraction of deep heat, can be understood by
240 considering the effect of core total heat capacity, which we vary widely. Finally, we assume that
241 mantle heat is transported only by conduction and thermal convection. Melting and melt
242 transport are not modeled, nor are the effects of an initial temperature gradient (e.g., a
243 superheated core). Our modeled evolutions provide a baseline view on which more complex
244 scenarios of heat transport can be evaluated.

245 Our approach permits a step toward understanding the influence of mantle layering on planetary
246 evolution, while also providing insight into when and how more complex processes might
247 interact with mantle layering. The importance of each additional complexity is not the same
248 across the different mantle structure scenarios, and so this work can guide future endeavors in
249 modeling layered systems. The implications of our work for systems closer to the complexity of
250 real planetary interiors are discussed in detail in Section 5.

251 **2.4 Model implementation:** We implemented the models of both temperature advection-
252 diffusion and material flow velocity using Lattice Boltzmann methods. This methodology
253 conceptualizes the physical world as statistically describable populations of particles that move
254 and interact on a grid, conserving momentum and energy (He and Luo, 1997). We use a multi-
255 distribution function approach to model thermal convection (Huber et al., 2008) with a heat
256 source based on the radiogenic heating rate. We also implement the buoyancy force (thermal
257 perturbation with temperature-dependent density leads to a body force $F = \rho g = \rho_0 g \alpha (T - T_0)$)
258 as in He and Luo (1998). We verified our implementations against analytical solutions to
259 simplified problems, as well as published numerical benchmarks for thermal convection
260 (Blankenbach et al., 1989); heat transport predicted by our model approached the benchmarked
261 values within 0.9% for Ra=10^4-10^6.

262 Lattice Boltzmann methods (LBM) are computationally efficient and can be both flexible
263 and simple to implement. However, LBM have not routinely been applied to geodynamical
264 problems in part because typical LBM implementations of thermal convection are generally
265 limited to a Prandtl number of approximately 1. Some LBM work has explored higher Prandtl

number simulations in which inertial and compressibility effects are negligible (Mora and Yuen, 2018; Chen et al., 2023) but this typically becomes computationally challenging because the numerical timestep must be very small in order to keep model velocities (and therefore Reynolds and Mach numbers) very small.

To approximate flow in the regime of large Prandtl number, as is appropriate for planetary mantles, we have developed a new technique to reduce the influence of inertia and compressibility. In summary, instead of using a very small time step, we achieve low velocities (and therefore low Mach and low Reynolds numbers) by scaling down forces and solving for the steady state velocity field. This approach is mathematically permissible because in the limit of incompressibility and infinite Prandtl number, Stokes flow is quasistatic, implying that the magnitude of velocities is exactly proportional to the magnitude of driving forces. For computational efficiency, we use a larger timestep for the momentum conservation solver than the heat transfer solver. We verified that this technique does not result in substantial difference in results for several model parameterizations.

The spatial resolution of our numerical model is chosen so that important features of the model, such as the convective boundary layers and the imposed layering in the model, are resolved with at least 7 nodes (most commonly at least 10); the grid size used in our models ranges from 100x424 to 200x1131. All models are run with an aspect ratio of $4\sqrt{2}$: 1 in the mobile region of the mantle to minimize the influence of box size on convective vigor when comparing different mantle structural scenarios. The temporal resolution of our models is chosen, in concert with the spatial resolution, to maintain the model velocities low enough to satisfy the Courant-Friedrichs-Lewy condition for stability (Courant et al., 1928).

3 Model results

We use variables extracted from timeseries data from the modeled planet evolutions to evaluate the consequences of mantle structure for planetary evolution as described by the relative timing of the four geologically important transitions: (1) the development of mantle convection, (2) the mantle cooling to subsolidus, (3) the onset of core cooling, and (4) the onset of net planet cooling. For each model planet, we track over time the maximum (over depth) horizontally

294 averaged advective heat flux in the mantle, the quantity of heat stored in the model mantle, and
295 the quantity of heat stored in the model core.

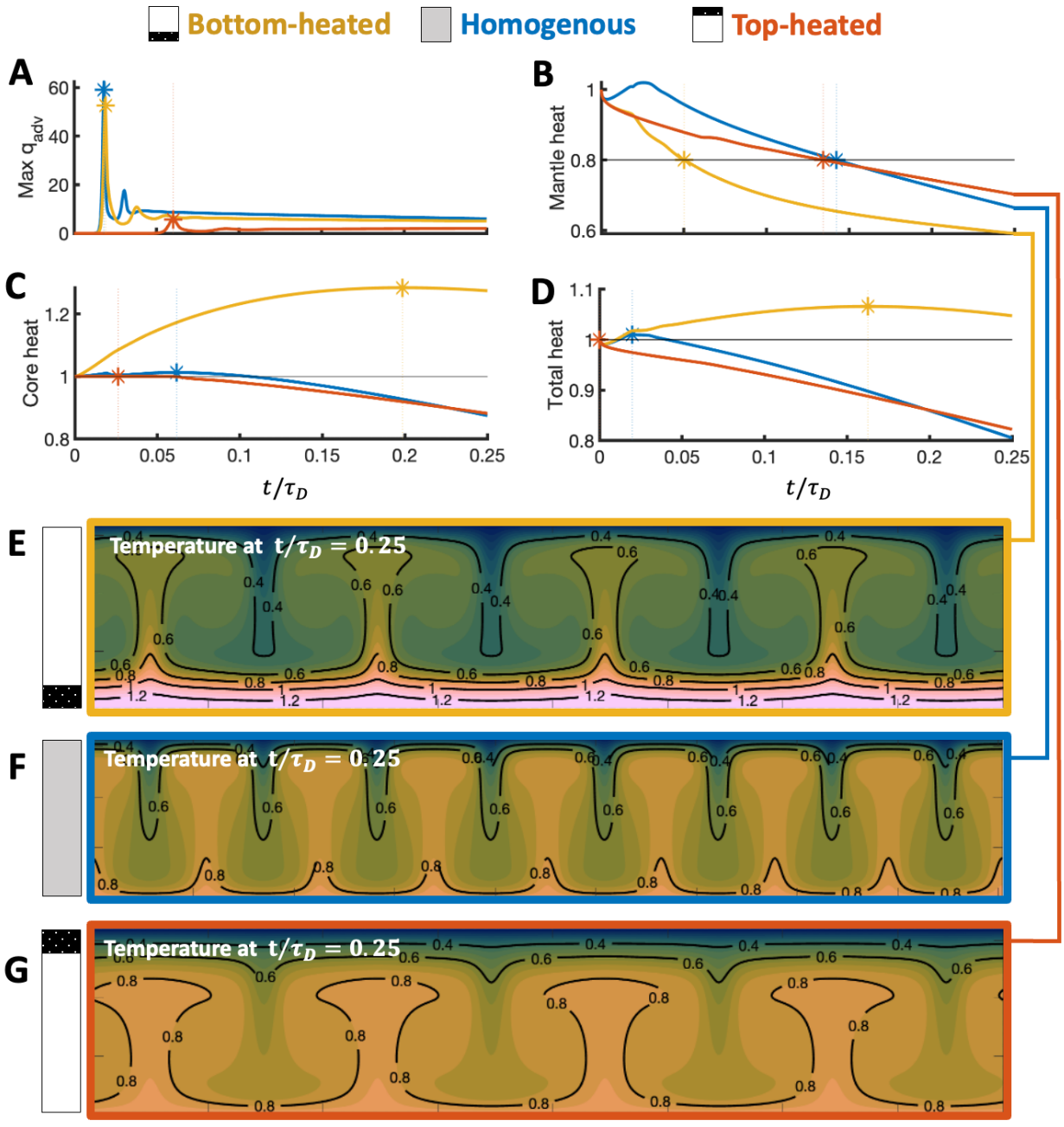

Figure 3. Timeseries results for an example trio of models ($Ra = 10^5$, initial $\tau_D/\tau_H = 11.5$, $d/L = 1/8, C = 2$). Panel (A) shows maximum horizontally averaged heat flux. Panel (B), (C), and (D) show mantle, core, and total planet heat, respectively. Stars indicate the geologically relevant timescale measured from the timeseries: development of convection in (A), time when average mantle temperature drops below 0.8 in (B), and transition from warming to cooling in (C) and (D). (E)-(G) show temperature field at $t/\tau_D = 0.25$ for each model.

296 As illustrated in Figure 3, we identify each of the four geological transitions of interest
297 with a feature measurable in these timeseries.

298 (1) Development of mantle convection: the first peak in advective heat flux (Figure 3A).

299 (2) Mantle cooling to subsolidus: the time when the mantle heat decreases to 80% of its initial
300 value (Figure 3B).

301 (3) and (4) Onset of net core and planet (core + mantle) cooling: the time of peak sensible
302 heat content of these thermal reservoirs (Figure 3C, 3D).

303 We note that all models experience a brief initial period of net planet cooling (see Figure
304 3D) as the initially thermally uniform mantle develops its upper thermal boundary layer. In order
305 to capture the long-term characteristics of the system, we choose a peak in heat content after the
306 cooling behavior is no longer dominated by this period of initial equilibration, which we define
307 to end when internal heat production would exceed top heat loss, assuming half-space cooling.
308 This ensures that we are capturing the effectiveness of transport of radiogenic heat by the system
309 rather than just the efficiency of heat loss by half-space cooling at the top of the mantle. This
310 also results in an initial decrease in mantle heat; we chose 80% of the initial heat as the model
311 threshold for a subsolidus mantle to be low enough to capture long-term evolutionary processes
312 rather than this short-term response to the initial conditions.

313 Timeseries of vertical heat flux and mantle, core, and planet heat and the derived
314 transition times are illustrated for a reference trio of model planets in Figure 3. In this example,
315 the simulations are run with identical Rayleigh number, core size, and total heat production (and
316 therefore they are energetically similar). They differ only in mantle structure; one is
317 homogenous, one has all HPE sequestered in a stabilized layer at the top of the mantle (top-
318 heated), and one has all HPE sequestered in a stabilized layer at the bottom of the mantle
319 (bottom-heated). In this reference trio, the evolution of the top-heated model exhibits a late (and
320 low) peak in advective heat flux compared to the other two scenarios but a relatively early onset
321 of planet and core cooling. The evolution of the bottom-heated model exhibits early development
322 of convection, similar to the homogenous scenario, but is different in that it experiences a
323 prolonged period of core and planet warming, while also losing heat from the mantle much
324 earlier than in the other two scenarios. These reference outputs are also characteristic of the
325 model results more broadly.

Figure 4 illustrates the relative timing of the four transitions of interest for our full suite of modeled evolutions; these times and the model parameterizations are also provided in Supplemental Table 1. Several features are particularly notable. Top-heated models exhibit early net planet and core cooling relative to the development of mantle convection, whereas homogenous and bottom-heated models develop convection at the same time as (or well before) the core and planet begin to cool down in all but the most sluggish, weakly heated cases. Top-heated and homogenous models experience net planet and core cooling before their mantles lose 20% of their initial sensible heat, whereas bottom-heated models display a range of behavior, with some losing mantle heat very early relative to the core (and overall planet) and others retaining it long after the core and planet have begun to cool down. It is worth noting that the duration of the period between the development of convection and the loss of 20% of the initial sensible heat of the mantle corresponds to the distance from the diagonal on these diagrams, so it can be seen that in many scenarios (those above the diagonal), the mantle gets cold enough to

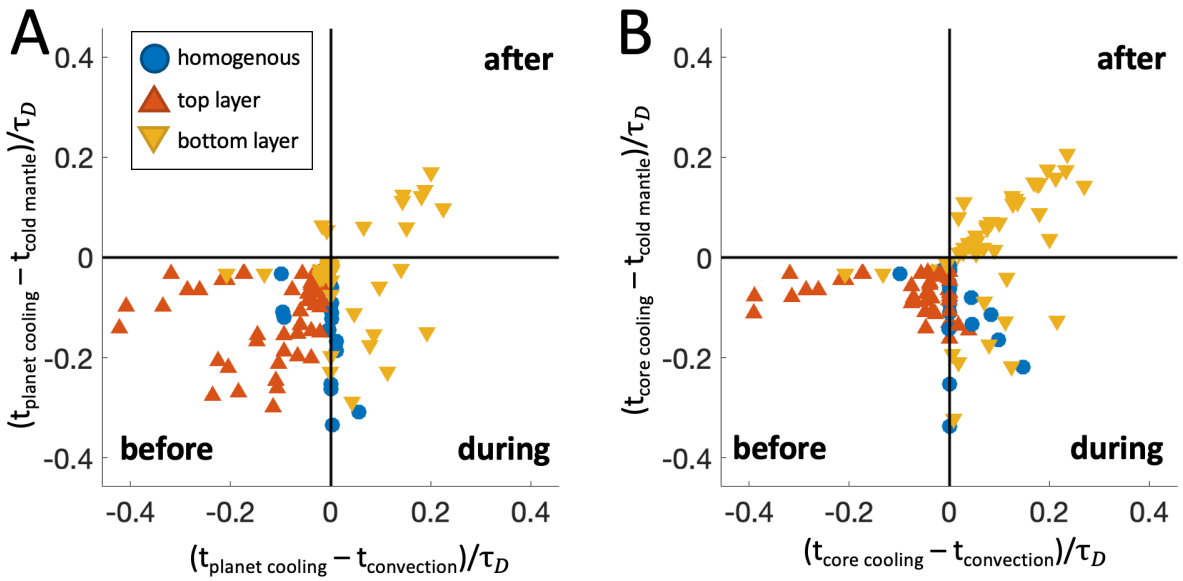

Figure 4. Timing of the transition from warming to cooling of model planets (A, $t_{planet\ cooling}$) and cores (B, $t_{core\ cooling}$) relative to the window for potential decompression melting, which we define to begin with the development of convection ($t_{convection}$) and end when the average mantle temperature drops below 0.8 ($t_{cold\ mantle}$). Timescales for all model evolutions are plotted excepting models which did not experience one of the relevant transitions within the time period modeled. Color indicates the scenario: homogenous are blue circles, top-heated are red, upward-pointing triangles, and bottom-heated are yellow, downward-pointing triangles. The quadrant within which a point falls indicates whether cooling begins **before**, **during**, or **after** the decompression melting window (labeled).

prevent partial melting before convection develops. These cases all have $Ra = 10^4$, which would be unrealistically low for a planet that is still hot.

The modeled evolutions are divided by mantle structure into different evolutionary regimes regarding the timing of net planet and core cooling relative to the window between the development of mantle convection and the loss of 20% of the initial mantle sensible heat, which can be taken as a proxy for the period of potential decompression melting. Most homogenous scenarios exhibit an onset of core and planet cooling at the beginning of this period, whereas the onset of core and planet cooling occurs before this period and during or after this period for top and bottom-heated scenarios respectively.

4 Discussion of Model Results

In this section, we discuss why the relative timing of the four geologically important transitions in our models depends so strongly on the mantle structure and the distribution of radiogenic elements.

4.1 Conceptual framework: Planets form with hot interiors due to the energy of accretion and differentiation (Kaula, 1979). Over time, this heat and the additional heat generated by radioactive decay is transported to the surface. In planets, as in our model, transport of heat is driven between the mantle and the surface, and between the core and mantle, by differences in temperature. Early on in evolution, the temperature difference between the mantle and the surface is much larger than that between the core and the mantle. As a result, heat is lost from shallower regions of the planet first; transport of heat from the core requires a temperature difference between the core and mantle, which requires loss of heat from the mantle.

The location of heat generation in a planet determines the relative timing of loss of radiogenic heat vs. original heat; the location of heat generation relative to insulation determines the magnitude of temperature differences necessary to cool the mantle and the core. Heat generated within the mantle replaces heat that is lost, limiting the development of a temperature difference between the core and mantle. Furthermore, when heat is dominantly transported by conduction across convective boundary layers and any stabilized layers (as opposed to volcanic heat-piping or plate recycling), heat generation within these layers increases the temperature difference necessary to transport heat from greater depths. Sensible heat can only be lost from

the mantle to the surface, or from the core to the mantle, through a heated layer if the temperature difference between the regions is sufficient to drive outward transport of all radiogenic heat produced in the layer. Similarly, sensible heat can only decrease in a volumetrically heated mantle when the temperature difference between the mantle and the surface drives heat transport at a rate which exceeds the rate of heat generation.

We can estimate the temperature difference across a layer which would drive heat flux in balance with heat production under the assumption of steady-state temperature variation within the layer (but with time-evolving boundary temperatures and heating rates). We frame this calculation in terms of timescales of heat production (τ_H) and heat transport (τ_t), defined below. Figure 5 illustrates how the balance of these two timescales gives the temperature difference necessary to drive loss of radiogenic heat. A larger temperature difference is required with stronger heat production (smaller τ_H) or less effective heat transport (larger τ_t), such as would occur with a thicker insulating layer. If the actual temperature difference between the mantle and the surface (or the core and the mantle) is larger than this calculated minimum, net cooling of the mantle (or core) is expected. If the actual temperature difference is s17maller, net warming is expected due to trapped radiogenic heat.

4.2 Physical framework: The heat production timescale, $\tau_H = \frac{\Theta C_m}{H_0}$, is the amount of time it would take to produce a reference quantity of heat (here, the initial sensible heat of the mantle, $Q_0 = \Theta C_m$). To build the heat transport timescale, τ_t, we define the conductive heat transport timescale τ_κ of a layer with thickness d to be the time it would take to transport that reference quantity of heat through the layer, assuming steady state, no heat production, and a driving temperature difference Θ; $\tau_\kappa = \tau_D \frac{d}{L}$, where τ_D is the diffusive timescale of the mantle. Then the heat transport timescale of a multi-layer, heated system (such as a stabilized layer over a convective boundary layer) is the sum of the conductive transport timescales of the individual layers, each multiplied by a factor F indicating the fraction of HPE that are below that layer (1 if all HPE are deeper, 0.5 if HPE are uniformly dispersed in the layer, 0 if all HPE are shallower); this factor accounts for the fact that heat is more easily lost when it is closer to the surface. Conceptually, τ_t is the timescale of loss of the produced heat. Mathematically, $\tau_t = \sum_i \tau_{\kappa,i} F_i$.

We can now relate the timescales of heat production and transport to the temperature difference necessary to drive loss of radiogenic heat by twice integrating equation (3) across the layers in question at time 0, assuming 1-D steady state and zero velocity. Integrating $\frac{\partial^2 T}{\partial z^2} + \frac{\tau_D}{\tau_H} \cdot f(z) = 0$ twice with the requirement that heat flux into the bottom of the layers (at z_0) must balance deeper heat production, we find that $\Delta T/\Theta = \frac{\tau_D}{\tau_H} \int_{z_0}^{z_1} \int_0^z f(x)dx\,dz$, where $\tau_t = \tau_D \int_{z_0}^{z_1} \int_0^z f(x)dx\,dz$. Values of τ_t for the configurations we model are illustrated and stated

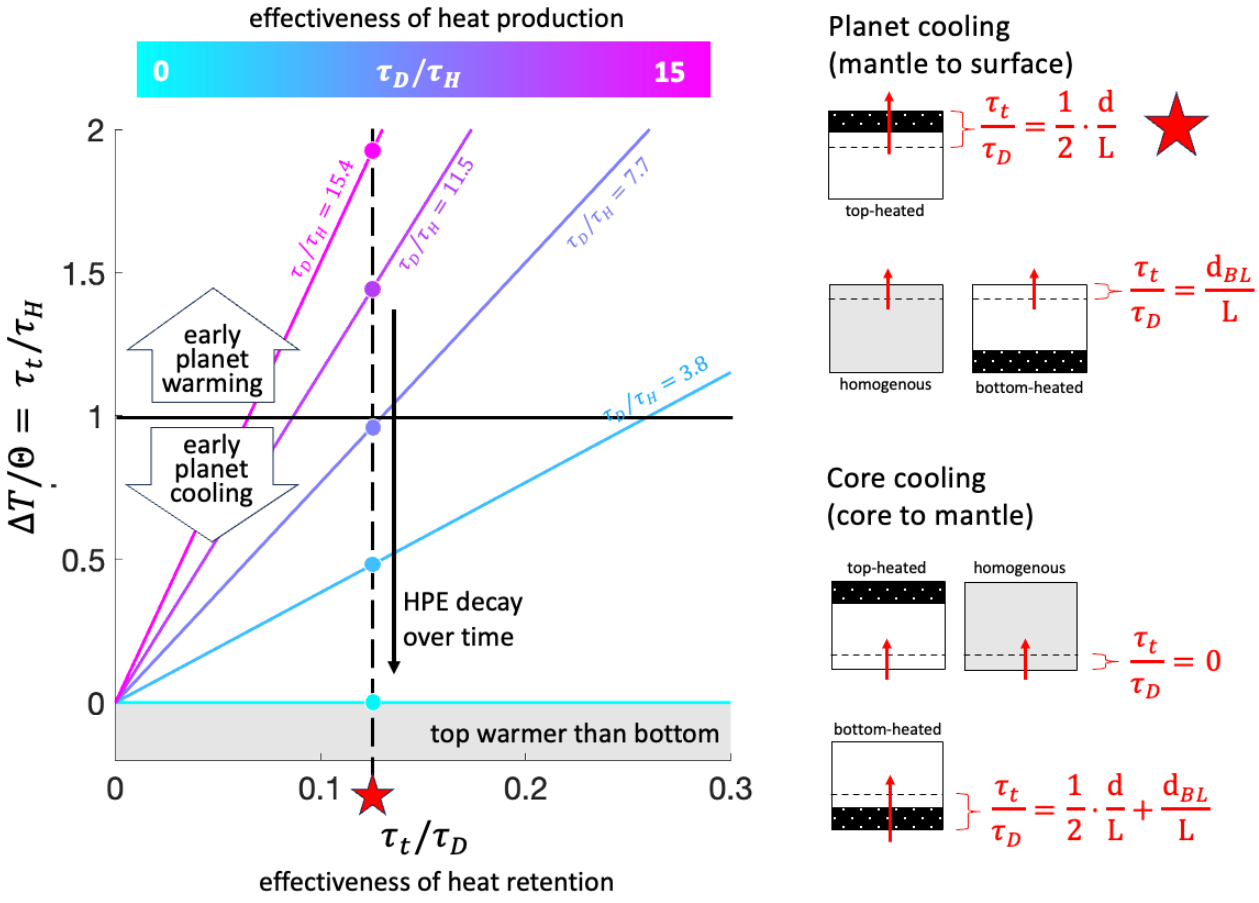

Figure 5. Temperature difference (normalized to reference temperature Θ) which drives heat transport in balance with production, as a function of the timescale of heat production, τ_H (higher means weaker heating), and the timescale of transport of that heat, τ_t (higher means more insulating). Color indicates heating strength; warmer colors indicate stronger heat production. Expressions for τ_t for model scenarios are given on the right. One example is illustrated for planetary cooling with the top ¼ of the mantle stabilized (so $\tau_t/\tau_D = 1/8$; dashed line). Since the initial normalized mantle temperature is equal to 1 (black solid line), initial planet warming is expected for the two most strongly heated cases ($\tau_D/\tau_H = 15.4$ and $\tau_D/\tau_H = 11.5$; dots above line), whereas initial planet cooling is expected for the three more weakly heated cases (dots below line). This is indeed observed (see Figure 6).

in Figure 5. Therefore, heat production and transport will balance when the driving temperature difference is simply equal to the ratio of the timescales (Figure 5):

We can use equation (5) to understand many aspects of our model behavior by carefully choosing which layers to describe. For example, to predict the onset of net planet cooling, we should describe the layers between the mantle interior and the surface: the upper convective boundary layer in the homogenous and bottom-heated scenarios ($\tau_t = \tau_{\kappa,BL}$) and additionally the stabilized layer in the top-heated scenario ($\tau_t = 0.5 \cdot \tau_{\kappa,\mathrm{l}} + 0 \cdot \tau_{\kappa,BL}$; zero in the second term because all HPE are above the convecting mantle). To predict the onset of core cooling, we should describe the layers between the core and mantle interior: the bottom convective boundary layer in the top-heated and homogenous scenarios ($\tau_t = 0 \cdot \tau_{\kappa,\mathrm{BL}}$ since approximately all HPE are above the boundary layer) and additionally the stabilized layer in the bottom-heated scenario ($\tau_t = \tau_{\kappa,\mathrm{BL}} + 0.5 \cdot \tau_{\kappa,\mathrm{l}}$). In our models, actual values for τ_t/τ_D range from approximately 0.05 to 0.5. We can also observe from equation (5) that insulation and heat production may have a similar effect on planetary heat transport, depending on their geometry.

4.3 Mantle-surface heat transport: We apply this framework to explain the behavior of our model, first considering the layers controlling heat transport between the mantle and the surface. This encompasses the stabilized layer in the top-heated case as well as the upper convective boundary layer. Since these layers control the rate of heat loss from the planet as well as from the mobile mantle, the timing of planet cooling and development of convection are controlled by the properties of the layers; these timescales as measured from our model results are plotted in Figure 6. We observe that for the homogenous and bottom-heated scenarios, convection develops early except in cases with barely super-critical Rayleigh numbers, while strong heating may delay planet cooling especially in the bottom-heated case. In contrast, the onset of convection in the top-heated case is delayed, often even in cases with high Ra number (akin to lower mantle viscosity), whereas the planet usually cools immediately.

Why does heat production delay convection but not planet cooling in the top-heated scenario, but have the opposite effect in the bottom-heated scenario? In the top-heated scenario, radiogenic heat produced in the stabilized layer must be lost before any sensible heat can be transferred upwards from the mobile mantle or deeper planet. Therefore, the transition to planet net cooling necessarily precedes the development of convection, which is suppressed by both the

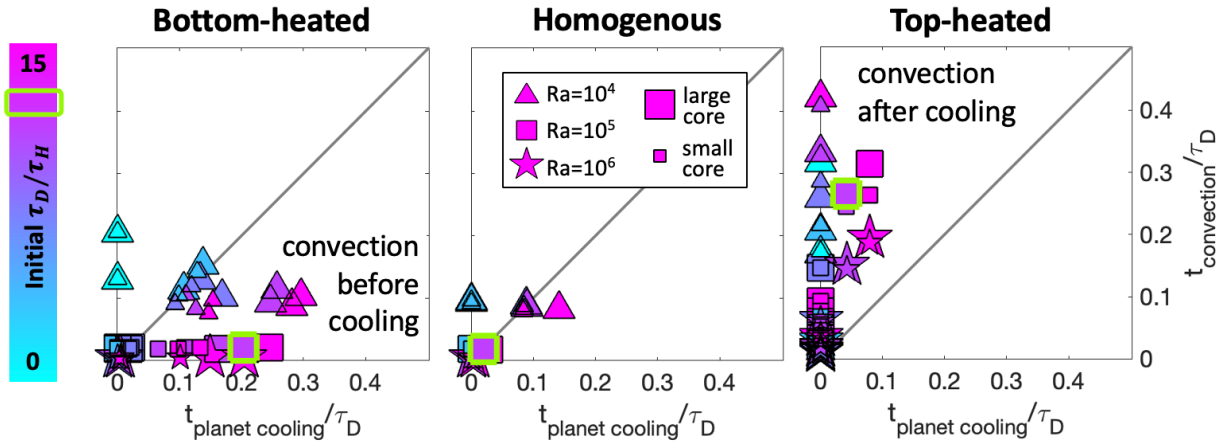

Figure 6. Time of transition from planet warming to cooling vs. time of development of convection for all models, separated by structural scenario (bottom-heated left, homogenous center, top-heated right). Each point indicates one model evolution. Marker colors indicate initial heating rate, with warmer colors indicating stronger heating; shape indicates Rayleigh number. Small markers indicate small cores. Figure 7 provides more data for points highlighted in green.

heating in the top layer and its stagnant nature. In the bottom-heated and homogenous cases, there is no barrier to loss of heat from the mobile mantle, so convection develops independently of the transition time from planet warming to cooling, delayed only by boundary layer development.

Why does strong radiogenic heat production delay the onset of planet net cooling most effectively in bottom-heated models? The planet is cooling overall when the temperature difference between the mantle and surface (ΔT_{ms}) is large enough to drive heat loss in excess of radiogenic production ($\Delta T_{ms}/\Theta > \tau_t/\tau_H$), and warming when the temperature difference is not large enough ($\Delta T_{ms}/\Theta < \tau_t/\tau_H$). The bottom-heated and homogenous models cover similar initial values for τ_t/τ_H and the mantle temperature; furthermore, heat production (the primary control on τ_t/τ_H) decreases exponentially with a fixed half-life in all models, and surface temperature is fixed. Therefore, the difference in behavior has to do with the time-evolution of the mantle temperature, illustrated in Figure 7. In homogenous cases, radiogenic heat warms the mantle, so the mantle temperature is increasing whenever the planet is warming. In the bottom-heated scenario, radiogenic heat is isolated from the convective mantle, so the mantle interior temperature decreases rapidly at first, whether the planet is warming or not, resulting in less effective heat transport. Consequently, the bottom-heated models experience longer periods of

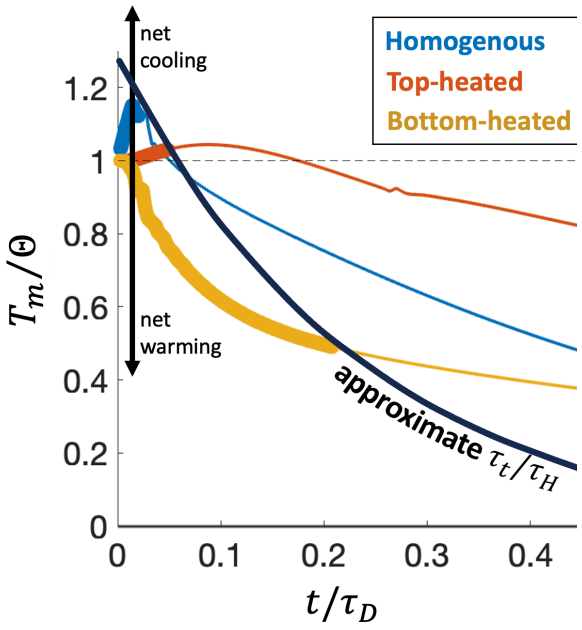

Figure 7. Time-evolution of mantle temperature (T_{ms}/Θ, equivalent to $\Delta T_{ms}/\Theta$) for an example model trio (Ra=10^5, initial τ_D/τ_H = 11.5, larger core, d=L/4, initial $\tau_t/\tau_H > 1$). ΔT_{ms} is measured from the center of the mobile mantle to the surface. Bolded sections of the curves indicate net warming.

warming; some even experience both early and late cooling when initially heat transport outstrips production but tapers off rapidly as the mantle temperature decreases.

4.4 Core-mantle heat transport: We now consider heat transport between the core and mantle. The structure of layers at the core-mantle boundary (the bottom convective boundary layer and any deep stabilized layer) controls the loss of core vs. mantle sensible heat, as driven by the temperature difference ΔT_{cm} across the layers. This is reflected in the time of the onset of core cooling relative to the time when the normalized mantle temperature drops below our chosen threshold of 0.8 (Figure 8). Unlike the bottom-heated scenario, the top-heated and homogenous scenarios lack heat production at the core-mantle boundary, so the core will cool as soon as the

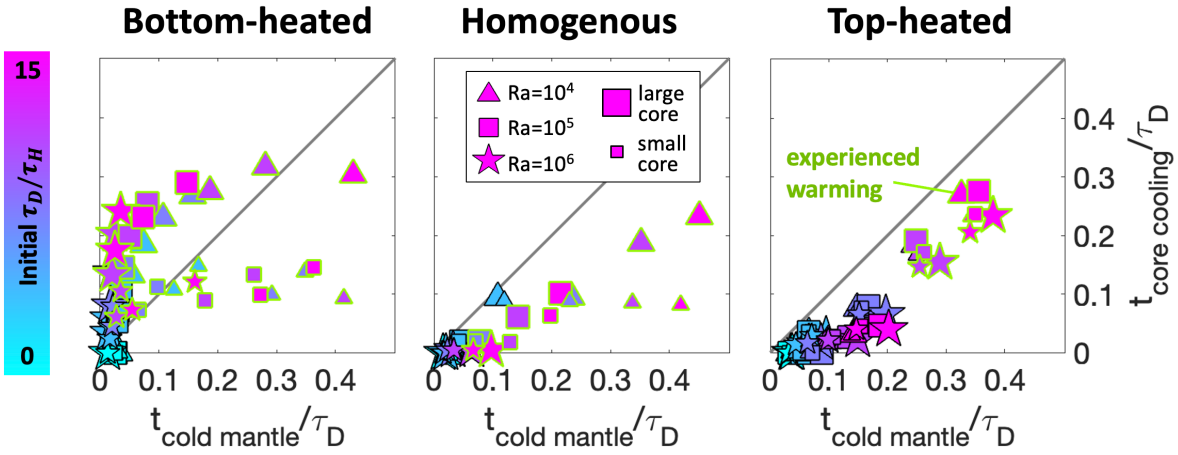

Figure 8. Time when (normalized) mantle temperature drops below 0.8 vs. time when core transitions from warming to cooling for all models, split by scenario (bottom-heated left, homogenous center, top-heated right). Symbology is same as in Figure 6, except that green outlines indicate the model planet experienced warming ($\tau_t/\tau_H > \Delta T_{ms}$ at some point).

mantle is colder than the core ($\Delta T_{cm} > 0$). In other words, core cooling is delayed only by early mantle warming and it commences as soon as excess mantle heat is removed. In contrast, for the bottom-heated scenario, the temperature difference between the core and mantle interior must be sufficiently large to drive loss of all radiogenic heat through both the stabilized layer and the bottom boundary layer of convection before the core can cool. The necessary temperature difference is larger than 0.2 for all our models with non-zero heat production. Consequently, the mantle temperature will necessarily drop below 80% of its initial temperature before the core can begin to cool (Figure 9) as long as the timescale of mantle temperature decrease (related to τ_t of the upper boundary) is small relative to the timescale of core temperature increase in response to top warming (related to core size).

4.5 Consequences of sequestered

HPE: By combining these insights, we can now explain why the relative timing of the four geologically important transitions in our models depends so strongly on the location of radiogenic elements. Mantle cooling and convection require net loss of shallow mantle heat; core cooling requires net loss of deep mantle heat; planet net cooling requires loss of radiogenic heat. Convection further requires development of a temperature difference across the mobile mantle. When HPE are sequestered in the shallow mantle, radiogenic heat must be removed before sensible heat can be lost from the mobile mantle or deeper. Therefore, the consequence of shallow HPE sequestration is an onset of net planet cooling and sometimes even core cooling before the development of convection (which marks the beginning of the era of possible decompression melting). In the most strongly

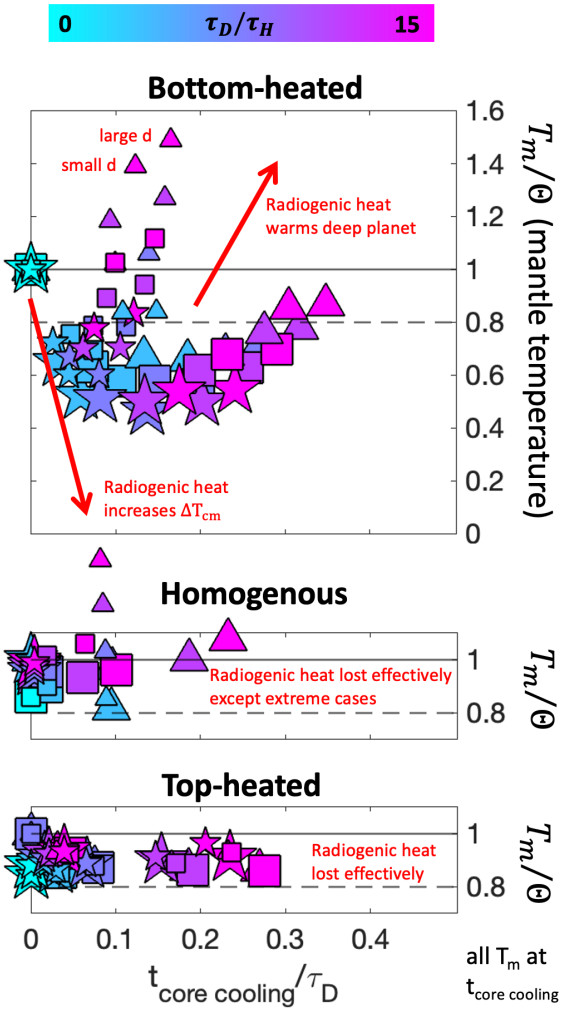

Figure 9. Mantle mean temperature at the time of the onset of core cooling for all models. Symbology is same as in Figure 6.

heated cases, the radiogenic half-life is the limiting timescale delaying the onset of convection, leading to the long delays seen in the model results. When HPE are sequestered in the deep mantle, the reverse is true: mantle sensible heat must be lost before radiogenic heat can be removed. Therefore, the core and sometimes also the planet can only transition from warming to cooling once a large quantity of heat has been lost from the mantle, often so much that the warming-cooling transitions happen after the convecting mantle has cooled to a very low temperature, after the era of possible decompression melting. Sensible heat removal takes time, leading to long delays in the onset of core cooling in bottom-heated cases.

In summary, the terrestrial planets contain two important regions through which heat is transferred by thermal conduction, one at the top and one at the bottom of the mantle. The structure of these regions, especially in terms of heat production and insulation, can strongly influence the relevant timescales of planetary cooling and related processes. The similarity in patterns of behavior between the bottom-heated and homogenous scenarios (with regard to planet cooling vs. convection) and between the top-heated and homogenous scenarios (with regard to mantle vs. core cooling) stem from the similarity in layering/heating at the top and bottom of the mantle, respectively.

5. Implications for planets

In this section, on the basis of our analysis, we offer predictions for the geological evolution of a typical top-heated vs. bottom-heated planet and discuss the possible relationships to, and implications for, Mercury, the Moon, and Mars.

Extrapolation from our model results to geological consequences requires care because of the simplifications made in the model. Conclusions from the model results are primarily based on the relative importance of heat generation and conductive heat transport at boundary layers at the top and bottom of the mantle. Since these layers are relatively thin and immobile, neither curvature nor variable mantle viscosity should affect our conclusions at least at a qualitative level; we also note that a stagnant lid would have a similar effect to that of an insulating crust. Melt production changes the relationship between energy change and temperature change, effectively buffering against mantle warming; we consider this effect qualitatively in the following discussion, but we note that extension of this work to quantitatively evaluate the interaction with melting in a similar framework would be a productive avenue of research. The

528 transport of potential heat by extraction of HPE-rich melt could be important, but we point out
529 that crust-building is simply a mechanism by which HPE become stably sequestered at the top of
530 the mantle. We do not expect transport of the sensible/latent heat of the melt to change our
531 conclusions qualitatively, since volcanism has transported far less total heat through the
532 lithosphere than conduction, except in planetary bodies exhibiting extreme activity (i.e., Io, and
533 perhaps Venus) (Solomon and Head, 1982).

534 **5.1 Geological history of a planet with shallow HPE:** In a planet with its HPE
535 sequestered at the top of its mantle (top-heated), our models predict contemporaneous global
536 contraction and potential for magnetic field generation and decompression melting (Figure 10A).
537 Therefore, volcanic units resulting from decompression melting would be younger than any
538 tectonic features related to global expansion but may be crosscut by compressional features;
539 furthermore, these units (or contemporaneous basins) may preserve a magnetic signature. The
540 surface expression of mantle melting may also be affected by the compressive stress state of the lithosphere (e.g., Wilson and Head, 2017).

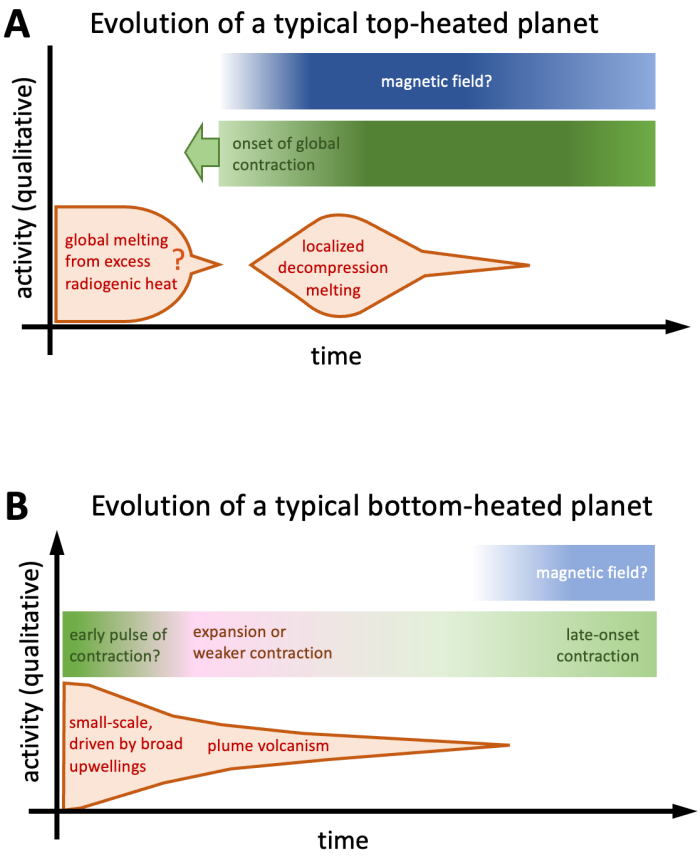

Figure 10. Sketch of predicted geological evolution for a typical top-heated (A) vs. bottom-heated (B) planet.

The delayed development of convection seen in our top-heated models indicates that radiogenic heat produced above the mobile mantle suppresses convection (as does the insulation of the stabilized layer); therefore, the vigor of convection in a top-heated planet would initially increase (perhaps from zero) as radioactive heat production declines. The opposite (declining convective vigor) is expected for a homogenous or bottom-heated planet. Volcanism in the absence of convection would be

559 possible in a top-heated planet if radiogenic heat in excess of that which can be conducted
560 through the crust resulted in melting (as has been suggested for the Moon; e.g., Wieczorek and
561 Phillips, 2000). A top-heated planet without initial excess radiogenic heat ($\tau_t/\tau_H < 1$) would
562 experience only a convection-driven volcanic phase. However, a top-heated planet with initial
563 excess radiogenic heat ($\tau_t/\tau_H > 1$) would have a volcanic record featuring two phases, possibly
564 separated by a lull in activity; net secular cooling leading to global contraction should begin
565 before the second phase. Volcanism driven by excess radiogenic heat vs. decompression would
566 likely differ in spatial distribution: globally distributed vs. concentrated over upwellings
567 respectively. Magmas would likely also be distinct in composition due to their different source
568 regions: late-stage magma ocean cumulates vs. the well-mixed mantle.

569 **5.2 Geological history of a planet with deep HPE:** For a planet with its HPE
570 sequestered at the bottom of its mantle (bottom-heated), our models predict early-onset mantle
571 convection which is initially driven by top-cooling, with bottom-heating becoming more
572 important over time (Figure 10B). The volcanic record might therefore feature a transition from
573 widespread, small-scale volcanism when top-cooling dominates, to plume-style volcanism later
574 on. Planet warming is expected with moderate HPE concentrations and would end during or after
575 the planet's volcanic era, implying that melting can occur when the lithosphere is in a state of
576 extensional stress. An initial pulse of global contraction is possible during early rapid cooling.

577 The potential for a magnetic field contemporaneous with volcanic activity depends
578 strongly on the response of the planet's core-mantle boundary temperature to heat production in
579 the lower mantle, since even weak heating in the lower mantle necessitates development of a
580 large temperature difference between the core and convective mantle. If the core temperature
581 increases quickly in response to deep mantle heat production (e.g., if the core is small), this
582 difference may be established by core warming while the planet is still volcanically active. If the
583 core temperature does not increase rapidly (e.g., if melting of the lower mantle is buffering
584 against temperature change), a magnetic field cannot exist until the mantle temperature drops
585 adequately. In this case, magnetic field generation may be possible only after the planet is
586 volcanically no longer active. If deep HPE partially melted the lower mantle, recrystallization
587 also buffers against core cooling. We note that this does not preclude a very early magnetic field
588 driven by cooling of an initially superheated core or colder overturned cumulates.

589 **5.3 Discussion of implications for Mercury, Moon, and Mars:** Mercury's geological
590 record bears several characteristics suggesting that the structure of its crust/shallow mantle
591 influenced its evolution. Volcanically, Mercury has a thick ancient crust (Padovan et al., 2015;
592 Marchi et al., 2013) as well as evidence of a distinct later pulse of more localized smooth plains
593 volcanism (Whitten et al., 2014; Byrne et al., 2016; Wang et al., 2021). Global contraction began
594 before the era of flood volcanism but after the ancient crust was built (Crane and Klimczak,
595 2017). Magnetic data suggest an early-onset, long-lived magnetic field which is also active today
596 (Hood et al., 2018). Alignment of these features with predictions for a top-heated planet (Figure
597 10A) lead us to hypothesize that a large fraction of Mercury's HPE are stably sequestered in its
598 upper mantle. Mercury's bulk chemistry could have produced a top-heated structure as fractional
599 crystallization of Mercury's magma ocean concentrated both sulfur and HPE into the remaining
600 melt (Boukare et al., 2019). More sophisticated geodynamical studies would be very helpful in
601 evaluating this hypothesis, which has not yet been considered directly. Future geochemical
602 analysis could also test this hypothesis via its implied prediction that the intercrater plains and
603 smooth plains represent radiogenically-driven and convection-driven eras of volcanism on
604 Mercury.

605 In contrast, Mars appears in several ways to be a prototypical bottom-heated planet, with
606 early intense volcanism that involves mantle plume activity (Carr and Head, 2009) but an absent
607 late-stage dynamo despite a liquid core (Acuna et al., 1999; Yoder et al., 2003), and an extended
608 era of weak contraction (Andrews-Hanna and Broquet, 2023). Broadly, evidence of long-term
609 bottom-heating of the mantle in the absence of evidence of long-term top-cooling of the core
610 suggests a heat source between them. Deep sequestration of HPE would be consistent with Mars'
611 oxidized bulk chemistry, which predicts high density final magma ocean cumulates (Elkins-
612 Tanton et al., 2003). Furthermore, results from the *Insight* mission suggest the presence of a
613 liquid silicate layer on top of the core of Mars, which could plausibly consist of molten HPE-rich
614 overturned cumulates (Samuel et al., 2020; Samuel et al., 2023; Khan et al., 2023); this would
615 indicate that Mars is in a large (thermally unresponsive) core regime, as explored in our models.
616 The long volcanic history of Mars suggests that HPE sequestration and insulation by the volcanic
617 crust are likely to be important as well, serving to slow mantle cooling while increasing overall
618 planet cooling (avoiding major expansion) by loss of crustal radiogenic heat.

619 The Moon's mare volcanism resembles Mercury's smooth plains volcanism in volume,
620 but differs in style, duration, and timing (Byrne et al., 2018; Head and Wilson, 2017; Head et al.,
621 2023). However, in contrast to Mercury's early-onset contraction, the Moon experienced an early
622 era of expansion (Solomon and Head, 1980; Andrews-Hanna et al., 2013) which transitioned to
623 surprisingly moderate contraction after peak mare volcanic flux (Nahm et al., 2023); relatively
624 late and gradual contraction aligns with deep sequestration of some HPE. On the basis of our
625 model results and comparison to Mercury and Mars, we suggest that the Moon's history
626 indicates deep sequestration of some HPE. This interpretation aligns with the conclusions of
627 previous work modeling the Moon's evolution as well as magma ocean solidification models
628 (Hess and Parmentier, 1995; Zhang et al., 2013). The possible present-day presence of a partially
629 molten layer at the base of the mantle (Khan et al., 2014) would also point to deeply sequestered
630 HPE. We note that the Moon's small core complicates interpretation of its magnetic history, but
631 a suggested long-lived early dynamo in either the Moon (Tikoo et al., 2017) or Mars (Mittleholz
632 et al., 2020) could be at odds with the hypothesis of deep HPE (Samuel et al., 2020). This
633 scenario requires further evaluation; a deep heated layer reduces transport of core heat to the
634 surface, but to what extent can a magnetic field be driven by transport of deep core heat to the
635 shallower core/planet?

636 Finally, while our discussion focused on Mercury, Mars, and the Moon, our results are
637 applicable to any planetary body in which thermal conduction is the dominant form of heat
638 transport between its core and mantle, and from its mantle to the surface. Our results scale
639 directly to aluminum-heated planetesimals with mantle thicknesses of a few 10's of km
640 ($\tau_D/\tau_H \approx 23$ at the time of solar system formation) or to approximately Earth-size thorium-
641 heated planets. More broadly, our qualitative results apply to planets in which volumetric heat is
642 delivered rapidly relative to the longest timescales of their evolution such as the mantle diffusive
643 timescale.

644 This work highlights several promising avenues of future investigation. The interaction of
645 heat production and insulation exhibited by top-heated models, as well as the core vs. mantle
646 control of the regime of radiogenic heat partitioning observed in the bottom-heated models, are
647 worth further characterization. Where are the boundaries of these regimes, and how are they
648 manifested in more complex systems? More detailed evaluation of the geological implications of
649 these simplified model results would be very productive as well; what pattern of volcanism

would be predicted for a Mercury-like planet with upward sequestration of HPE, and does it match the spatiotemporal pattern observed on Mercury? What magnetic and volcanic evolution would be predicted for Mars if its deep mantle sequestered HPE, considering the interaction of basal melting and development of a conductive region in its core? Can a similar framework be used to evaluate the consequences of other perturbations to the thermochemical state of a planetary body, such as foundering of KREEP material in the Moon (Elkins-Tanton et al., 2002) after an early era of accumulation of radiogenic heat?

6. Conclusions

The small terrestrial bodies (Mercury, the Moon, and Mars) exhibit similar themes of volcanism, tectonism, and magnetic field generation, but with very different rates of activity over time. We have presented our evaluation of the influence of stabilized sequestration of heat-producing elements (HPE) at the top or bottom of a planet's mantle on its geological evolution. We explored numerically the behavior of a simplified model of a planet with a layered mantle, focusing on the timing of four geologically important transitions: the development of mantle convection, the cooling of the mantle below its solidus, the onset of core cooling, and the onset of net planet cooling. We found mantle structure to be an important control on the timing and especially on the relative timing of these events in the model.

As compared to models with a homogenous and fully mobile mantle, in which cooling and convection are strongly coupled, we found that stabilized upward sequestration of HPE results in a regime of thermal evolution where HPE decay and the conductive evolution of the top layer is more important for the overall evolution than convective redistribution of deeper heat. We observe the onset of net planet cooling and core cooling before the development of convection in almost all cases. Stabilized downward sequestration of HPE results in longer-term retention of heat.

We believe these results to be robust, even in light of the many simplifications of the model. Our conclusions align with previous work which finds that downward sequestration of HPE explains aspects of the evolution and present-day state of Mars and the Moon. We suggest that upward sequestration of HPE should be further considered as a factor in the evolution of Mercury.

Acknowledgments

L. Lark, C. Huber, and E. M. Parmentier were supported by NASA Emerging Worlds grant 80NSSC22K0634.

Open Research

Results of model runs are included in Supplemental Table 1. The code used to execute the models will be made available via zenodo. It is currently available to reviewers here: https://github.com/lhp/planetary_evolution.

References

Acuna, M. H., Connerney, J. E. P., Ness, Lin, R. P., Mitchell, D., Carlson, C. W., ... & Cloutier, P. (1999). Global distribution of crustal magnetization discovered by the Mars Global Surveyor MAG/ER experiment. Science, 284(5415), 790-793.

Andrews-Hanna, J. C., Asmar, S. W., Head III, J. W., Kiefer, W. S., Konopliv, A. S., Lemoine, F. G., ... & Zuber, M. T. (2013). Ancient igneous intrusions and early expansion of the Moon revealed by GRAIL gravity gradiometry. Science, 339(6120), 675-678.

Andrews-Hanna, J. C., & Broquet, A. (2023). The history of global strain and geodynamics on Mars. Icarus, 395, 115476.

Blankenbach, B., Busse, F., Christensen, U., Cserepes, L., Gunkel, D., Hansen, U., ... & Schnaubelt, T. (1989). A benchmark comparison for mantle convection codes. Geophysical Journal International, 98(1), 23-38.

Boukaré, C. E., Parman, S. W., Parmentier, E. M., & Anzures, B. A. (2019). Production and preservation of sulfide layering in Mercury's mantle. Journal of Geophysical Research: Planets, 124(12), 3354-3372.

Byrne, P. K., Klimczak, C., Celâl Şengör, A. M., Solomon, S. C., Watters, T. R., & Hauck, II, S. A. (2014). Mercury's global contraction much greater than earlier estimates. Nature Geoscience, 7(4), 301-307.

Byrne, P. K., Ostrach, L. R., Fassett, C. I., Chapman, C. R., Denevi, B. W., Evans, A. J., ... & Solomon, S. C. (2016). Widespread effusive volcanism on Mercury likely ended by about 3.5 Ga. Geophysical Research Letters, 43(14), 7408-7416.

Byrne, P. K., Whitten, J. L., Klimczak, C., McCubbin, F. M., & Ostrach, L. R. (2018). The volcanic character of Mercury. Mercury. The View after MESSENGER, 287-323.

Carr, M. H., & Head III, J. W. (2010). Geologic history of Mars. Earth and Planetary Science Letters, 294(3-4), 185-203.

714 Cartier, C., & Wood, B. J. (2019). The role of reducing conditions in building Mercury.
715 Elements: An International Magazine of Mineralogy, Geochemistry, and Petrology,
716 15(1), 39-45.

717 Chen, S., Luo, K. H., Jain, A. K., Singh, D., & McGlinchey, D. (2023). Natural convection of
718 large Prandtl number fluids: A controversy answered by a new thermal lattice Boltzmann
719 model. Case Studies in Thermal Engineering, 44, 102827.

720 Courant, R., Friedrichs, K., & Lewy, H. (1928). Über die partiellen Differenzengleichungen der
721 mathematischen Physik. Mathematische annalen, 100(1), 32-74.

722 Crane, K. T., & Klimczak, C. (2017). Timing and rate of global contraction on Mercury.
723 Geophysical Research Letters, 44(7), 3082-3089.

724 ELKINS-TANTON, L. T., Parmentier, E. M., & Hess, P. C. (2003). Magma ocean fractional
725 crystallization and cumulate overturn in terrestrial planets: Implications for Mars.
726 Meteoritics & Planetary Science, 38(12), 1753-1771.

727 Elkins-Tanton, L. T., Zaranek, S. E., Parmentier, E. M., & Hess, P. C. (2005). Early magnetic
728 field and magmatic activity on Mars from magma ocean cumulate overturn. Earth and
729 Planetary Science Letters, 236(1-2), 1-12.

730 He, X., & Luo, L. S. (1997). Lattice Boltzmann model for the incompressible Navier–Stokes
731 equation. Journal of statistical Physics, 88, 927-944.

732 Head, J. W., & Wilson, L. (2017). Generation, ascent and eruption of magma on the Moon: New
733 insights into source depths, magma supply, intrusions and effusive/explosive eruptions
734 (Part 2: Predicted emplacement processes and observations). Icarus, 283, 176-223.

735 Head, J. W., Wilson, L., Hiesinger, H., van der Bogert, C., Chen, Y., Dickson, J. L., ... & Ziyuan,
736 O. (2023). Lunar mare basaltic volcanism: Volcanic features and emplacement processes.
737 Reviews in Mineralogy and Geochemistry, 89(1), 453-507.

738 Hess, P. C., & Parmentier, E. M. (1995). A model for the thermal and chemical evolution of the
739 Moon's interior: Implications for the onset of mare volcanism. Earth and Planetary
740 Science Letters, 134(3-4), 501-514.

741 Hood, L. L., Oliveira, J. S., Galluzzi, Valentina, & Rothery, D. A. (2018). Investigating sources
742 of Mercury's crustal magnetic field: Further mapping of MESSENGER magnetometer
743 data. Journal of Geophysical Research: Planets, 123(10), 2647-2666.

744 Huber, C., Parmigiani, A., Chopard, B., Manga, M., & Bachmann, O. (2008). Lattice Boltzmann
745 model for melting with natural convection. International Journal of Heat and Fluid Flow,
746 29(5), 1469-1480.

747 Johnson, C. L., Phillips, R. J., Purucker, M. E., Anderson, B. J., Byrne, P. K., Denevi, B. W., ...
748 & Solomon, S. C. (2015). Low-altitude magnetic field measurements by MESSENGER
749 reveal Mercury’s ancient crustal field. Science, 348(6237), 892-895.

750 Kaula, W. M. (1979). Thermal evolution of Earth and Moon growing by planetesimal impacts.
751 Journal of Geophysical Research: Solid Earth, 84(B3), 999-1008.

752 Kellogg, L. H., Hager, B. H., & van der Hilst, R. D. (1999). Compositional stratification in the
753 deep mantle. Science, 283(5409), 1881-1884.

754 Khan, A., Connolly, J. A., Pommier, A., & Noir, J. (2014). Geophysical evidence for melt in the
755 deep lunar interior and implications for lunar evolution. Journal of Geophysical Research:
756 Planets, 119(10), 2197-2221.

757 Khan, A., Huang, D., Durán, C., Sossi, P. A., Giardini, D., & Murakami, M. (2023). Evidence
758 for a liquid silicate layer atop the Martian core. Nature, 622(7984), 718-723.

759 Marchi, S., Chapman, C. R., Fassett, C. I., Head, J. W., Bottke, W. F., & Strom, R. G. (2013).
760 Global resurfacing of Mercury 4.0–4.1 billion years ago by heavy bombardment and
761 volcanism. Nature, 499(7456), 59-61.

762 Mittelholz, A., Johnson, C. L., Feinberg, J. M., Langlais, B., & Phillips, R. J. (2020). Timing of
763 the martian dynamo: New constraints for a core field 4.5 and 3.7 Ga ago. Science
764 Advances, 6(18), eaba0513.

765 Mora, P., & Yuen, D. A. (2018). Simulation of regimes of convection and plume dynamics by
766 the thermal Lattice Boltzmann Method. Physics of the Earth and Planetary Interiors, 275,
767 69-79.

768 Nahm, A. L., & Schultz, R. A. (2011). Magnitude of global contraction on Mars from analysis of
769 surface faults: Implications for martian thermal history. Icarus, 211(1), 389-400.

770 Nahm, A. L., Watters, T. R., Johnson, C. L., Banks, M. E., van der Bogert, C. H., Weber, R. C.,
771 & Andrews-Hanna, J. C. (2023). Tectonics of the Moon. Reviews in Mineralogy and
772 Geochemistry, 89(1), 691-727.

773 Ness, N. F. (1979). The magnetic field of Mercury. Physics of the Earth and Planetary Interiors,
774 20(2-4), 209-217.

775 Padovan, S., Wieczorek, M. A., Margot, J. L., Tosi, N., & Solomon, S. C. (2015). Thickness of
776 the crust of Mercury from geoid-to-topography ratios. Geophysical Research Letters,
777 42(4), 1029-1038.

778 Peterson, G. A., Johnson, C. L., & Jellinek, A. M. (2021). Thermal evolution of Mercury with a
779 volcanic heat-pipe flux: Reconciling early volcanism, tectonism, and magnetism. Science
780 Advances, 7(40), eabh2482.

781 Plesa, A. C., Padovan, S., Tosi, N., Breuer, D., Grott, M., Wieczorek, M. A., ... & Banerdt, W. B.
782 (2018). The thermal state and interior structure of Mars. Geophysical Research Letters,
783 45(22), 12-198.

784 Plesa, A. C., Tosi, N., & Breuer, D. (2014). Can a fractionally crystallized magma ocean explain
785 the thermo-chemical evolution of Mars?. Earth and Planetary Science Letters, 403, 225-
786 235.

787 Samuel, H., Ballmer, M. D., Padovan, S., Tosi, N., Rivoldini, A., & Plesa, A. C. (2021). The
788 thermo-chemical evolution of Mars with a strongly stratified mantle. Journal of
789 Geophysical Research: Planets, 126(4), e2020JE006613.

790 Samuel, H., Drilleau, M., Rivoldini, A., Xu, Z., Huang, Q., Garcia, R. F., ... & Banerdt, W. B.
791 (2023). Geophysical evidence for an enriched molten silicate layer above Mars's core.
792 Nature, 622(7984), 712-717.

Solomon, S. C. (1978). On volcanism and thermal tectonics on one-plate planets. Geophysical Research Letters, 5(6), 461-464.

Solomon, S. C., & Head, J. W. (1980). Lunar mascon basins: Lava filling, tectonics, and evolution of the lithosphere. Reviews of Geophysics, 18(1), 107-141.

Stegman, D. R., Jellinek, A. M., Zatman, S. A., Baumgardner, J. R., & Richards, M. A. (2003). An early lunar core dynamo driven by thermochemical mantle convection. Nature, 421(6919), 143-146.

Tanton, L. T. E., Van Orman, J. A., Hager, B. H., & Grove, T. L. (2002). Re-examination of the lunar magma ocean cumulate overturn hypothesis: melting or mixing is required. Earth and Planetary Science Letters, 196(3-4), 239-249.

Thomas, R. J., Rothery, D. A., Conway, S. J., & Anand, M. (2014). Long-lived explosive volcanism on Mercury. Geophysical Research Letters, 41(17), 6084-6092.

Tikoo, S. M., & Evans, A. J. (2022). Dynamos in the inner solar system. Annual Review of Earth and Planetary Sciences, 50, 99-122.

Tikoo, S. M., Weiss, B. P., Shuster, D. L., Suavet, C., Wang, H., & Grove, T. L. (2017). A two-billion-year history for the lunar dynamo. Science Advances, 3(8), e1700207.

Tosi, N., & Padovan, S. (2021). Mercury, Moon, Mars: Surface Expressions of Mantle Convection and Interior Evolution of Stagnant-Lid Bodies. Mantle convection and surface expressions, 455-489.

Tosi, N., Plesa, A. C., & Breuer, D. (2013). Overturn and evolution of a crystallized magma ocean: A numerical parameter study for Mars. Journal of Geophysical Research: Planets, 118(7), 1512-1528.

Wang, Y., Xiao, Z., Chang, Y., Xu, R., & Cui, J. (2021). Short-Term and Global-Wide Effusive Volcanism on Mercury Around 3.7 Ga. Geophysical Research Letters, 48(20), e2021GL094503.

Warren, P. H., & Wasson, J. T. (1979). The origin of KREEP. Reviews of Geophysics, 17(1), 73-88.

Watters, T. R., & Nimmo, F. (2010). The tectonics of Mercury. Planetary tectonics, 11, 15.

Watters, T. R., Selvans, M. M., Banks, M. E., Hauck, S. A., Becker, K. J., & Robinson, M. S. (2015). Distribution of large-scale contractional tectonic landforms on Mercury: Implications for the origin of global stresses. Geophysical Research Letters, 42(10), 3755-3763.

Werner, S. C. (2009). The global martian volcanic evolutionary history. Icarus, 201(1), 44-68.

Whitten, J. L., Head, J. W., Denevi, B. W., & Solomon, S. C. (2014). Intercrater plains on Mercury: Insights into unit definition, characterization, and origin from MESSENGER datasets. Icarus, 241, 97-113.

Wieczorek, M. A., & Phillips, R. J. (2000). The “Procellarum KREEP Terrane”: Implications for mare volcanism and lunar evolution. Journal of Geophysical Research: Planets, 105(E8), 20417-20430.

Wilson, L., & Head, J. W. (2017). Generation, ascent and eruption of magma on the Moon: New insights into source depths, magma supply, intrusions and effusive/explosive eruptions (Part 1: Theory). Icarus, 283, 146-175.

Yoder, C. F., Konopliv, A. S., Yuan, D. N., Standish, E. M., & Folkner, W. M. (2003). Fluid core size of Mars from detection of the solar tide. Science, 300(5617), 299-303.

Zhang, N., Dygert, N., Liang, Y., & Parmentier, E. M. (2017). The effect of ilmenite viscosity on the dynamics and evolution of an overturned lunar cumulate mantle. Geophysical Research Letters, 44(13), 6543-6552.

Zhang, N., Parmentier, E. M., & Liang, Y. (2013). Effects of lunar cumulate mantle overturn and megaregolith on the expansion and contraction history of the Moon. Geophysical Research Letters, 40(19), 5019-5023.